# Molecular Simulation of Complete Phase Diagrams for Binary Mixtures

**Monica H. Lamm and Carol K. Hall**
Dept. of Chemical Engineering, North Carolina State University, Raleigh, NC 27695

*Vapor-liquid, vapor-solid and liquid-solid coexistence lines are calculated for binary mixtures of Lennard-Jones spheres using Monte Carlo simulation and the Gibbs-Duhem integration technique. Complete phase diagrams showing equilibrium between vapor, liquid and solid phases are constructed for binary Lennard-Jones mixtures with diameter ratios ranging from $\sigma_{11}/\sigma_{22} = 0.85 - 1.0$ and attractive well-depth ratios ranging from $\epsilon_{11}/\epsilon_{22} = 0.625 - 1.6$, at a reduced pressure $P^* \equiv P\sigma_{11}^3/\epsilon_{11} = 0.002$. The Lorentz-Berthelot combining rules are used to calculate the cross-species interaction parameters $\sigma_{12}$ and $\epsilon_{12}$. The variation in the shape of the complete phase diagrams change as a function of the diameter ratio $\sigma_{11}/\sigma_{22}$ and well-depth ratio $\epsilon_{11}/\epsilon_{22}$ is systematically explored. The phase diagrams found here resemble those found experimentally for argon-methane, iodine-sulfur, water-sodium chloride, water-silver nitrate, water-potassium nitrate, and p-dichlorobenzene-p-dibromobenzene.*

## Introduction

Knowledge of the phase behavior of mixtures is crucial to the successful design and operation of countless processes encountered in chemical engineering practice. Design engineers need to know, for example, whether they will encounter precipitates in pipelines, liquid-liquid separation in a distillation column, or cosolvency in a supercritical fluid extraction column. Although the phase equilibrium of a mixture can, in principle, be measured at any condition of interest, ultimately, one would like to be able to predict mixture phase behavior based solely upon knowledge of the components' molecular architecture and intermolecular forces.

The prediction of phase equilibria for mixtures has been the subject of intensive investigation for decades. Two kinds of studies have been conducted: (1) those aimed at developing accurate predictions of phase equilibria for specific substances (such as hydrocarbon mixtures, polar/nonpolar mixtures, and so on), and (2) those aimed at providing general intuition about the overall topography of phase diagrams for broad classes of substances, with particular focus on how intermolecular forces impact phase diagram shape. The latter type of study is exemplified by the work of Scott and van Konynenburg (1970) and van Konynenburg and Scott (1980), who analyzed how the types of phase diagrams predicted by the van der Waals equation of state for binary mixtures depend on the values of the van der Waals size and energy parameters. Remarkably, the simple van der Waals equation of state was found to exhibit five of the six types of fluid phase behavior observed experimentally. This landmark study has been followed by similar analyses for other equations of state, such as the Redlich-Kwong (Deiters and Pegg, 1989), the Carnahan-Starling-Redlich-Kwong (Kraska and Deiters, 1992), the Guggenheim (Wang et al., 2000), and the Ree (Mazur et al., 1984) equations of state.

Most of the research aimed at understanding how intermolecular interactions affect phase behavior has focused exclusively on fluid-phase equilibria. However, in real systems, solid phases form and often interrupt the complex phase behavior exhibited by fluids (Schneider, 1978; Scott, 1987). Many phenomenological descriptions of complete phase behavior (that is, showing equilibrium between vapor, liquid, and solid phases) have been given, beginning with Smits (1903) and Bakhuis Roozeboom and Buchner (1905), who recognized that there are two types of solid-fluid-phase behavior in binary mixtures (not to be confused with the six-types of fluid-phase behavior classified by van Konynenburg and Scott). In Type 1, the three-phase solid-liquid-vapor coexistence curve does not interfere with the liquid-vapor critical curve. In Type 2, the three-phase solid-liquid-vapor curve does interfere with the liquid-vapor critical curve; the intersection of these two curves forms critical endpoints where the critical liquid and

Correspondence concerning this article should be addressed to C. K. Hall.

vapor phases coexist in the presence of a solid. Based on these two general types of solid-fluid behavior, Valyashko (1986, 1990) proposed a classification scheme for twelve types of complete diagrams. Eight of these types result from the analysis of experimental data for water-inorganic salt mixtures. The remaining four types were deduced by the method of continuous topological transformation, which involves making educated guesses about the transitions in topography between the eight known types. This method is based on the idea that there are continuous transitions between all types of phase behavior (Schneider, 1970). Luks (1980) and Peters et al. (1986) have qualitatively described four types of complete phase diagrams observed for binary mixtures of solvent (methane, ethane, carbon dioxide) and a homologous series of solutes ($n$-alkanes).

A quantitative description of complete phase behavior has been given by Luks and coworkers (Garcia and Luks, 1999; Labadie et al., 2000). Garcia and Luks (1999) calculate the solid-liquid-vapor locus for binary mixtures of solvent and a homologous series of solutes using the van der Waals equation of state for the fluid phase and a simple fugacity model for the solid phase. This work was extended by Labadie et al. (2000), who calculated the fluid-phase critical loci for these mixtures, offering a picture of how the multiphase topography progresses with changes in the solute properties. They found examples of solid-fluid phase behavior in keeping with what has been observed in real systems, as well as solid-fluid phase behavior that has yet to be verified by experiment. As with any analytical equation of state, there exists the possibility that the new topographies are mathematical artifacts stemming from the approximations made in the development of the equation of state. Nonetheless, the new possibilities for complete phase behavior calculated by Luks and coworkers are intriguing and invite further investigation.

The most accurate way to determine how molecular size, shape, and energy of interaction influence phase equilibria is with molecular simulation, since molecular simulations provide exact results for the model system being studied (Allen and Tildesley, 1987). A significant advance was made in the simulation of phase equilibria when Panagiotopoulos (1987, 1988) introduced the Gibbs ensemble method. In this method, the two coexisting phases are simulated independently, yet are coupled thermodynamically in order to satisfy the criteria of phase equilibrium: equal temperatures, pressures, and species chemical potentials. These conditions are satisfied by simulating each phase at the same temperature and pressure, and performing particle transfers between the phases to maintain chemical potential equality.

Although the Gibbs ensemble method has been widely adopted for studying fluid-phase equilibria, it is not an efficient method for studying solid-phase equilibria because a large number of successful particle transfers between each phase are required for chemical potential equilibration. Inspired by the Gibbs ensemble method, Kofke (1993) introduced the Gibbs-Duhem integration technique for direct simulation of phase equilibria. As in the Gibbs ensemble method, two or more coexisting phases are simulated independently at the same temperature and pressure. However, instead of using particle transfers, the chemical potential equality among each phase is maintained by integrating along the Clapeyron differential equation for coexistence during the simulations. Eliminating the need for particle transfers between phases makes the Gibbs-Duhem integration method well-suited for calculating phase equilibrium for cases in which one of the phases is a solid. The method requires an initial coexistence condition to begin the integration of the Clapeyron equation; this initial condition can be obtained from simulation data (such as a Gibbs ensemble simulation or a previous Gibbs-Duhem integration), a reliable theory, or experimental data.

The focus of most of the simulations of vapor-liquid and liquid-liquid phase behavior has been the Lennard-Jones fluid, the quintessential model of a system containing spherically symmetric molecules. The Lennard-Jones intermolecular potential is given by

$$u_{ij}(r) = 4\epsilon_{ij}\left[\left(\frac{\sigma_{ij}}{r}\right)^{12} - \left(\frac{\sigma_{ij}}{r}\right)^{6}\right], \tag{1}$$

where $u_{ij}$ is the potential energy of interaction between particles $i$ and $j$, $r$ is the distance between particles $i$ and $j$, $\epsilon_{ij}$ is the Lennard-Jones attractive well-depth, and $\sigma_{ij}$ is the Lennard-Jones diameter. Simulations of the fluid-phase behavior for Lennard-Jones mixtures have proven useful for testing theories (Georgoulaki et al., 1994; Harismiadis et al., 1991; Tsang et al., 1995), as well as for developing general intuition regarding the influence of molecular size and intermolecular interactions on phase behavior (Canongia Lopes, 1999; Canongia Lopes and Tildesley, 1997; Guo et al., 1994; van Leeuwen et al., 1991; Sadus, 1999).

In a previous article (Hitchcock and Hall, 1999) we used the Gibbs-Duhem integration method combined with semi-grand canonical Monte Carlo simulations to calculate solid-liquid phase diagrams for binary Lennard-Jones mixtures over a range of diameter ratios $\sigma_{11}/\sigma_{22} = 0.85$–$1.0$ and well-depth ratios $\epsilon_{11}/\epsilon_{22} = 0.45$–$1.6$. The cross-species interaction parameters were calculated using the Lorentz-Berthelot (Rowlinson and Swinton, 1982) combining rules. We found that for well-depth ratios of unity (equal attractions among species), phase behavior indicative of eutectics and solid solutions with minimum melting points is observed for diameter ratios ranging from 0.85 to 1. We then varied the well-depth ratio of the mixtures at several constant diameter ratios and observed transitions from solid solution to solid solution with a minimum melting point, from solid solution with a minimum melting point to eutectic, and from solid solution to peritectic. Using our simulation results, we were able to map out the boundaries separating regimes of solid solution, solid solution with a minimum melting point, eutectic, and peritectic solid-liquid phase behavior in the space spanned by the Lennard-Jones diameter and well-depth ratios.

More recently, we have demonstrated that the Gibbs-Duhem integration method can be used to calculate complete phase diagrams (Hitchcock and Hall, 2000; Lamm and Hall, 2000) where by "complete" we mean containing all possible phases: solid, liquid, and vapor. Prior to that, complete phase diagrams for symmetric (equal diameters, $\sigma_{11} = \sigma_{22}$; equal attractive well-depths, $\epsilon_{11} = \epsilon_{22}$) Lennard-Jones mixtures were calculated by Vlot et al. (1997) using a combination of molecular simulation and semiempirical models. In their work, Monte Carlo simulations were conducted for each phase at selected state points to determine the excess free energy as a function of composition. The resulting free energy vs. composition data was fit with a two-parameter

Redlich-Kister polynomial and the convex envelope construction method was used to determine the phase diagram. In comparison to this somewhat indirect method, the Gibbs-Duhem integration method can be applied to the calculation of complete phase diagrams with relative ease.

Our objective in this article is to explore the effect of both molecular size and intermolecular attractions on the complete phase behavior of a mixture. We calculate complete phase diagrams for binary Lennard-Jones mixtures with diameter ratios ranging from 0.85–1.0 and attractive well-depth ratios ranging from 0.625–1.6, at a reduced pressure $P^* \equiv P\sigma_{11}^3/\epsilon_{11} = 0.002$, which is equivalent to atmospheric pressure for argon. The cross-species interaction parameters are obtained from Lorentz-Berthelot combining rules. We restrict ourselves to diameter ratios ranging from 0.85 to 1.0, because calculations on binary hard-sphere mixtures have shown that the stable solid phase in this region is a substitutionally disordered fcc crystal (Barrat et al., 1986, 1987; Kranendonk and Frenkel, 1991; Cottin and Monson, 1995). At diameter ratios less than 0.85, the phase equilibrium calculation is more complex because several ordered crystalline phases are possible, necessitating the calculation of each phase's free energy to determine the most stable crystalline structure. Vapor-liquid, solid-liquid, and solid-vapor lines are calculated for each mixture by integrating the Clapeyron differential equation for binary mixture phase equilibria at constant pressure. The initial conditions for the integrations are the vapor-liquid and fcc solid-liquid coexistence data for a single component Lennard-Jones system at $P^* = 0.002$ obtained via Gibbs-Duhem integration (Kofke, 1993; Agrawal and Kofke, 1995). The properties of each phase at subsequent integration points are determined by semigrand canonical Monte Carlo simulations (constant temperature, pressure, total number of molecules, and fugacity fraction) on the vapor, liquid, and solid phases.

Highlights of our results are the following. We find that, for well-depth ratios of unity (equal attractions among species), there is no interference between the vapor-liquid and solid-liquid coexistence regions. As the well-depth ratio increases or decreases from unity, the vapor-liquid and solid-liquid phase envelopes widen and interfere with each other leading to a solid-vapor coexistence region. For all well-depth ratios and a diameter ratio of 0.95, the solid-liquid lines have a shape characteristic of a solid solution (with or without a minimum melting temperature); as the diameter ratio decreases, the solid-liquid lines fall to lower temperatures until they eventually drop below the solid-solid coexistence region, resulting in either a eutectic or peritectic three-phase line. These phase diagrams presented here resemble those found experimentally for argon-methane, iodine-sulfur, water-sodium chloride, water-silver nitrate, water-potassium nitrate, and *p*-dichlorobenzene-*p*-dibromobenzene.

The remainder of the article is organized as follows. The Gibbs-Duhem integration method is outlined and the procedure for the calculation of mixture phase behavior for solid, liquid, and vapor phases is described. The complete phase diagrams are then presented followed by a discussion of the results, followed by a brief summary and further discussion.

## Gibbs-Duhem Integration

In this section we describe how we calculated phase equilibria for binary Lennard-Jones mixtures using the Gibbs-Duhem integration method. We begin by presenting a brief review of the Gibbs-Duhem integration method. We then discuss our procedures for determining an initial coexistence condition and integrating the Clapeyron equation. Finally, we describe the details of the semigrand ensemble simulations used throughout the integration procedure to determine the properties of each of the coexisting phases.

The coexistence lines were calculated using Gibbs-Duhem integration (Kofke, 1993, 1998). In this method, phase coexistence is determined by numerically integrating the Clapeyron differential equation appropriate to the system of interest. Clapeyron equations describe how field variables (variables that must be equal among coexisting phases) change along the phase equilibrium line. The Clapeyron equation for equilibrium between two phases ($\alpha$ and $\gamma$) of a binary mixture containing components 1 and 2 at constant pressure is

$$\frac{d\beta}{d\xi_2} = \frac{(x_2^\alpha - x_2^\gamma)}{\xi_2(1-\xi_2)(h^\alpha - h^\gamma)}, \tag{2}$$

where $\beta$ is the reciprocal temperature $1/kT$, with $k$ the Boltzmann constant and $T$ the absolute temperature, $\xi_2$ is the fugacity fraction of species 2, $\xi_2 \equiv \hat{f}_2/\Sigma\hat{f}_i$, with $\hat{f}_i$, the fugacity of species $i$ in solution, $x_2$ is the mole fraction of species 2, and $h$ is the molar enthalpy. The righthand side of Eq. 2 can be integrated numerically to find an equation for $\beta$ as a function of $\xi_2$ if we have an initial condition describing the temperature, fugacity fraction, enthalpies and compositions at one coexistence point.

### *Initial condition*

An initial coexistence condition is necessary to begin a Gibbs-Duhem integration calculation for phase equilibrium in a binary mixture. A convenient choice for the initial coexistence condition is the vapor-liquid or solid-liquid equilibrium condition for either of the pure Lennard-Jones components. Here, we used literature data obtained via Gibbs-Duhem integration for the vapor-liquid (Kofke, 1993) and solid-liquid (Agrawal and Kofke, 1995) coexistence conditions. The integrand in Eq. 2 is undefined for pure components ($\xi_2 = 0$, $x_2 = 0$ and $\xi_2 = 1$, $x_2 = 1$), but it can be estimated using the limiting case of infinite dilution. Here, we follow Mehta and Kofke (1994), who used the infinite dilution case to start their Gibbs-Duhem integration calculations of vapor-liquid equilibria in binary mixtures.

The limiting value of the integrand when $x_2$ approaches zero $(d\beta/d\xi_2)_{x_2=0}$ can be estimated by supposing that the real mixture displays ideal solution behavior at the limit of infinite dilution of species 2. With this assumption, the abundant component (species 1) in the ideal solution follows the Lewis Randall rule

$$\hat{f}_1 = x_1 f_1, \tag{3}$$

while the dilute component (species 2) obeys Henry's law

$$\hat{f}_2 = x_2 H_2, \tag{4}$$

where $f_1$ is the fugacity of pure component 1 at the temperature and pressure of the mixture, and $H_2$ is the Henry's law

constant for species 2. Letting $x_1 \to 1$ and $x_2 \to 0$, the fugacity fraction of species 2 becomes, $\xi_2 = x_2 H_2/f_1$. After making these substitutions into Eq. 2 and rearranging terms (Hitchcock and Hall, 1999), we get

$$\left.\frac{d\beta}{d\xi_2}\right|_{x_2=0} = \frac{f_1(1/H_2^{\alpha} - 1/H_2^{\gamma})}{(h^{\alpha} - h^{\gamma})}. \tag{5}$$

This gives us an estimate for the integrand at the initial condition of $\xi_2 = 0$ and coexistence (for example, solid-liquid, vapor-liquid) temperature, $T_1$, of pure species 1. A similar formula can be derived in the limit of infinite dilution of species 1.

We can calculate all of the quantities on the righthand side of Eq. 5 with an NPT simulation of pure species 1. The molar enthalpy of each phase is $h = \langle u + Pv \rangle_{\mathrm{NPT}}$, where $u$ is the configurational energy of the system and the brackets $\langle\rangle_{\mathrm{NPT}}$ denote an NPT ensemble average. The quantity $f_1/H_2$ can be calculated from (Mehta and Kofke, 1994)

$$\frac{f_1}{H_2} = \langle \exp(-\beta \Delta u_{1\to 2}) \rangle_{\mathrm{NPT}} \tag{6}$$

where $\Delta u_{1\to 2}$ is the exchange energy associated with switching a particle from species 1 to 2. The exchange energy $\Delta u_{1\to 2}$ can be obtained by conducting trial identity switches during the simulation; these involve randomly selecting a particle and calculating the energy that would result if we were to switch the particle from species 1 to species 2. This is done without actually changing the particle's identity.

### *Integration*

Once we have an initial coexistence condition, the Gibbs-Duhem integration procedure may be performed over the entire range of fugacity fractions, $\xi_2 = 0$ to $\xi_2 = 1$, using a predictor-corrector algorithm to integrate Eq. 2. Starting at the initial condition $\beta_0$, $(\xi_2)_0$ we step to the next fugacity fraction $(\xi_2)_1$ and estimate the associated reciprocal temperature $\beta_1$ using the trapezoid-rule predictor formula

$$\beta_1^{(0)} = \beta_0 + [(\xi_2)_1 - (\xi_2)_0] F(\beta_0, (\xi_2)_0), \tag{7}$$

where the superscript 0 indicates that $\beta_1^{(0)}$ (a predicted value) is our zeroth iteration attempt at finding the reciprocal temperature $\beta_1$ and $F$ is the righthand side of Eq. 2 evaluated at the initial condition. Once $\beta_1^{(0)}$ is estimated at the given fugacity fraction $(\xi_2)_1$, two semigrand canonical (NPT$\xi_2$) Monte Carlo simulations (one for the $\alpha$ phase and one for the $\gamma$ phase) are conducted in order to calculate the enthalpies and mole fractions of each phase at the new state point. (Details of the NPT$\xi_2$ simulations will be given in the next subsection.)

After the enthalpies and mole fractions at the new state point are calculated, we refine the estimate for $\beta_1$ at $(\xi_2)_1$ by performing a loop of corrector iterations until $\beta_1$ converges within an acceptable tolerance. The general form of the trapezoid-rule corrector for this loop is given by

$$\beta_1^{(i+1)} = \beta_0 + \frac{[(\xi_2)_1 - (\xi_2)_0]}{2} \times \left[F_1^{(i)}(\beta_1^{(i)}, (\xi_2)_1) + F_0(\beta_0, (\xi_2)_0)\right], \tag{8}$$

where the superscripts $(i)$ and $(i+1)$ denote the iterations of the corrector, the subscripts 0 and 1 denote the initial and current state point, respectively, and $F_1^{(i)}$ is calculated from simulation averages of the enthalpies and mole fractions during the $i$th iteration of the corrector at $\beta_1^{(i)}$ and $(\xi_2)_1$. After $\beta_1$ converges, a production segment of simulations are run to obtain the final average enthalpies and mole fractions for the coexistence point. Once the production runs are completed, the fugacity fraction is incremented and the predictor-corrector algorithm described above is repeated to obtain the next state point $\beta_2$ $(\xi_2)_2$.

Higher-order predictor-corrector equations are used as we obtain more state points. The midpoint predictor-corrector is used once two state points are known

$$\beta_{n+1}^{(0)} = \beta_{n-1} + 2[(\xi_2)_{n+1} - (\xi_2)_n] F_n(\beta_n, (\xi_2)_n), \tag{9}$$

$$\beta_{n+1}^{(i+1)} = \beta_{n-1} + \frac{[(\xi_2)_{n+1} - (\xi_2)_n]}{3}\left[F_{n+1}^{(i)} + 4F_n + F_{n-1}\right], \tag{10}$$

and the modified Adams predictor-corrector (Carnahan et al., 1969) is used once three or more state points are known

$$\beta_{n+1}^{(0)} = \beta_n + \frac{[(\xi_2)_{n+1} - (\xi_2)_n]}{24} \times [55F_n - 59F_{n-1} + 37F_{n-2} - 9F_{n-3}], \tag{11}$$

$$\beta_{n+1}^{(i+1)} = \beta_n + \frac{[(\xi_2)_{n+1} - (\xi_2)_n]}{24} \times \left[9F_{n+1}^{(i)} + 19F_n - 5F_{n-1} + F_{n-2}\right]. \tag{12}$$

In these sets of equations, the predictor is listed first and the corrector second. The subscripts denote the coexistence state points with $(n+1)$ being the current state point and the superscripts denote the iterations of the corrector for the current coexistence state point. By repeating the predictor-corrector algorithm from $\xi_2 = 0$ to $\xi_2 = 1$, we can map out the entire temperature vs. composition phase diagram.

In some of the mixtures, we encountered interference between two different two-phase coexistence regions. For instance, much of the time the vapor-liquid and solid-liquid coexistence curves overlapped, resulting in a three-phase solid-liquid-vapor coexistence line. In this case, two Gibbs-Duhem integrations were conducted, the first starting from the vapor-liquid coexistence temperature for one of the pure components and the second starting from the solid-liquid coexistence temperature for the same pure component. For example, in Figure 1 vapor-liquid and solid-liquid coexistence curves can be calculated starting from the vapor-liquid and solid-liquid coexistence temperatures ($T_2^{lv}$ and $T_2^{ls}$, respectively) of pure component 2. At some $\xi_2$ (unknown at the commencement of the two integrations), the liquid-phase co-

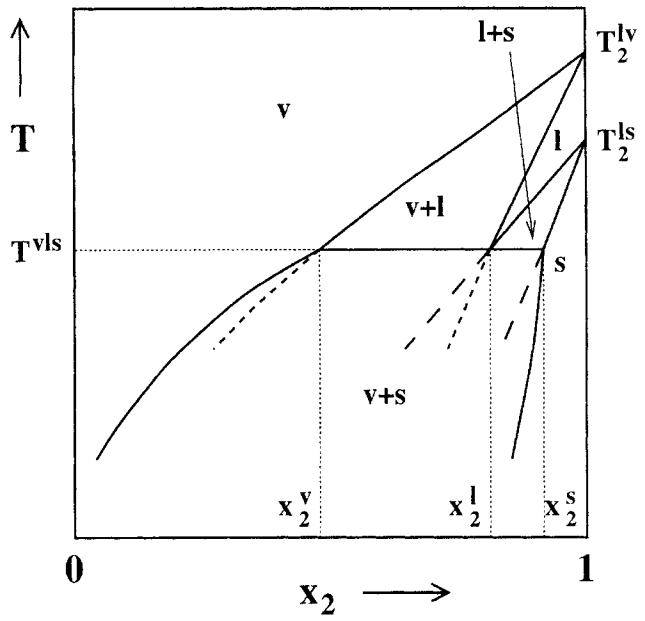


**Figure 1. Procedure used to determine a solid-liquid-vapor coexistence line.**

Solid lines show the equilibrium-phase boundaries on the $T - x_2$ diagram. The labels $v$ (vapor), $l$ (liquid), and $s$ (solid) identify the phases present in each region. Short-dashed and long-dashed lines represent the metastable parts of the vapor-liquid and solid-liquid coexistence curves, respectively. Other labels are as follows: $T_2^{lv}$, vapor-liquid coexistence temperature for component 2; $T_2^{ls}$, solid-liquid coexistence temperature for component 2; $T^{vls}$, vapor-liquid-solid coexistence temperature; $x_2^v$, $x_2^l$, $x_2^s$, the vapor, liquid, and solid-phase coexistence mol fractions for component 2.

existence lines from each set of coexistence curves will cross, thus, determining the temperature, fugacity fraction, and coexistence compositions of the three coexisting phases: vapor, liquid, and solid. In Figure 1 the liquid lines cross at $T^{vls}$ and $x_2^l$. Below $T^{vls}$, the inner vapor-liquid and solid-liquid coexistence curves (shown by short-dashed and long-dashed lines, respectively) are metastable with respect to the outer vapor-solid coexistence curves, according to the boundary curvature rule (Gordon, 1983; Prince 1966), which states that the boundaries of one-phase regions must meet at a three-phase line with curvatures such that the boundaries extrapolate into the two-phase coexistence regions. (It has been suggested that the boundary curvature rule given by Gordon is a variation of Schreinemaker's rule. We have investigated several sources on Schreinemaker's rule as applied to invariant triple points and quadruple points in pressure vs. temperature space but cannot find a clear connection between this theorem and the boundary curvature rule for the case discussed above.) The vapor-solid coexistence curve is determined by a Gibbs-Duhem integration starting from $T^{vls}$ at $x_2^v$ and $x_2^s$. Other types of three-phase coexistence lines (heteroazeotropes, eutectics, and so on) can be determined in a similar manner.

### *Simulations*

The enthalpies and mole fractions needed as input to the integration of Eq. 2 are obtained from semigrand canonical (constant NPT$\xi_2$) Monte Carlo computer simulations (Kofke and Glandt, 1988). In this work, all simulations were run with a system size of 500 particles at a reduced pressure $P^* = 0.002$. The temperature and fugacity fraction were fixed at the values specified by the Gibbs-Duhem integration predictor-corrector algorithm. There are three types of Monte Carlo trial moves in semigrand canonical simulations: particle displacements, volume change moves, and particle identity exchanges. The particle displacements and volume change moves are conducted just as they are in a standard NPT simulation (Allen and Tildesley, 1987). In the particle identity exchange moves a particle is selected at random and given a trial species identity switch, which is accepted according to the ratio of the species fugacity fractions $\xi_1$ and $\xi_2$. The overall acceptance probability (Mehta and Kofke, 1994) for the moves in the NPT$\xi_2$ ensemble is min[1,exp($\Lambda$)] where

$$\Lambda = -\beta(U^{\text{trial}} - U^{\text{old}}) - \beta P(V^{\text{trial}} - V^{\text{old}}) + N \ln \frac{V^{\text{trial}}}{V^{\text{old}}} + m \ln \frac{\xi_2}{1-\xi_2}. \quad (13)$$

In Eq. 13, $U^{\text{trial}}$ and $U^{\text{old}}$, and $V^{\text{trial}}$ and $V^{\text{old}}$ are the configurational energies and volumes of the trial and existing states, respectively, $m = +1$ if the trial identity switch is from species 1 to 2, and $m = -1$ if the trial identity switch is from species 2 to 1. In NPT$\xi_2$ simulations the choice of the type of Monte Carlo move is made randomly, but weighted, such that the ratio of attempted moves is 1 volume change to $N$ particle displacements to $N$ identity switches. The length of the simulation is given in cycles, where one cycle represents 1 volume change attempt, $N$ displacement attempts, and $N$ identity switch attempts. In our work, a typical NPT$\xi_2$ simulation is equilibrated for 3,000 cycles and then followed by a production run of 5,000 cycles to compute the average enthalpy and mole fraction. The only difference between fluid- and solid-phase simulations is that, to maintain an fcc crystalline structure in the solid-phase simulations, we impose a single occupancy constraint (Hansen and Verlet, 1969; Kofke, 1991) on the trial displacements of particles in the solid, that is, any displacements that put the particle outside its lattice cell are rejected.

Other details of the NPT$\xi_s$ simulations are as follows. The simulation volume is a cubic box with periodic boundary conditions. The particles interact via the Lennard-Jones potential model. We determine the cross-species interaction parameters ($\sigma_{12}$,$\epsilon_{12}$) by using the Lorentz-Berthelot (Rowlinson and Swinton, 1982) mixing rules $\sigma_{12} = (\sigma_{11} + \sigma_{22})/2$ and $\epsilon_{12} = \sqrt{\epsilon_{11}\epsilon_{22}}$. The potential interactions are truncated at a cutoff radius of half the box length. To compensate for this truncation, a long-range correction is applied to the energy calculations during the simulation by assuming a uniform density distribution beyond the cutoff radius (Allen and Tildesley, 1987).

## Results

In this section, we present the results of our Gibbs-Duhem integration calculations of complete phase behavior for bi-

nary Lennard-Jones mixtures. All of the phase diagrams were calculated at reduced pressure $P^* \equiv P\sigma_{11}^3/\epsilon_{11} = 0.002$, which is equivalent to atmospheric pressure for argon. We calculated a series of 11 phase diagrams for diameter ratios $\sigma_{11}/\sigma_{22} = 0.85$, 0.9, 0.95, and 1.0, and well-depth ratios $\epsilon_{11}/\epsilon_{22} = 0.625$, 1.0, and 1.6 (the phase diagram for $\sigma_{11}/\sigma_{22} = 1.0$ and $\epsilon_{11}/\epsilon_{22} = 1.0$ is trivial and will not be discussed). For these diameter ratios, the solid phase has a substitutionally disordered fcc crystalline structure. We begin with a detailed description of the phase diagrams found at $\sigma_{11}/\sigma_{22} = 0.95$ and then simply highlight the salient features of the remaining eight phase diagrams.

In the first series, we calculated phase diagrams for binary mixtures with $\sigma_{11}/\sigma_{22} = 0.95$ and $\epsilon_{11}/\epsilon_{22} = 0.625$, 1.0, and 1.6. Figure 2 shows the temperature-composition phase diagrams obtained via Gibbs-Duhem integration (row 1) along with not-to-scale schematic diagrams (row 2) drawn to illustrate the smaller features of the actual phase diagram more clearly. On the phase diagram for $\sigma_{11}/\sigma_{22} = 0.95$ and $\epsilon_{11}/\epsilon_{22} = 0.625$, vapor-liquid coexistence lines originate from pure component 2 ($x_2 = 1$, $T^* \equiv kT/\epsilon_{11} = 1.141$) and decrease in temperature with decreasing fugacity fraction $\xi_2$. Solid-liquid coexistence lines originate from pure component 2 ($x_2 = 1$, $T^* = 1.099$) and decrease in temperature with decreasing fugacity fraction $\xi_2$. The liquid-vapor and solid-liquid curves meet at $T^* = 1.093$ and form a three-phase, solid-liquid-vapor equilibrium line. Solid-vapor coexistence lines originate from this three-phase line and decrease in temperature with decreasing fugacity fraction $\xi_2$. Vapor-liquid curves originate from pure component 1 ($x_2 = 0$, $T^* = 0.732$) and increase in temperature with increasing fugacity fraction $\xi_2$. The vapor-liquid and vapor-solid curves meet at $T^* = 0.745$ and form a three-phase, vapor-liquid-solid equilibrium line. Liquid-solid coexistence lines originate from this three-phase line and decrease in temperature with decreasing fugacity fraction $\xi_2$ until they reach the solid-liquid coexistence temperature for pure component 1 ($x_2 = 0$, $T^* = 0.687$). A miscible solid phase exists below the solid-liquid curves.

On the phase diagram for $\sigma_{11}/\sigma_{22} = 0.95$ and $\epsilon_{11}/\epsilon_{22} = 1.0$, vapor-liquid coexistence lines originate from pure component 2 ($x_2 = 1$, $T^* = 0.742$) and decrease in temperature with decreasing fugacity fraction until they reach the vapor-liquid coexistence temperature for pure component 1 ($x_2 = 0$, $T^* = 0.732$). A miscible liquid phase exists below the vapor-liquid

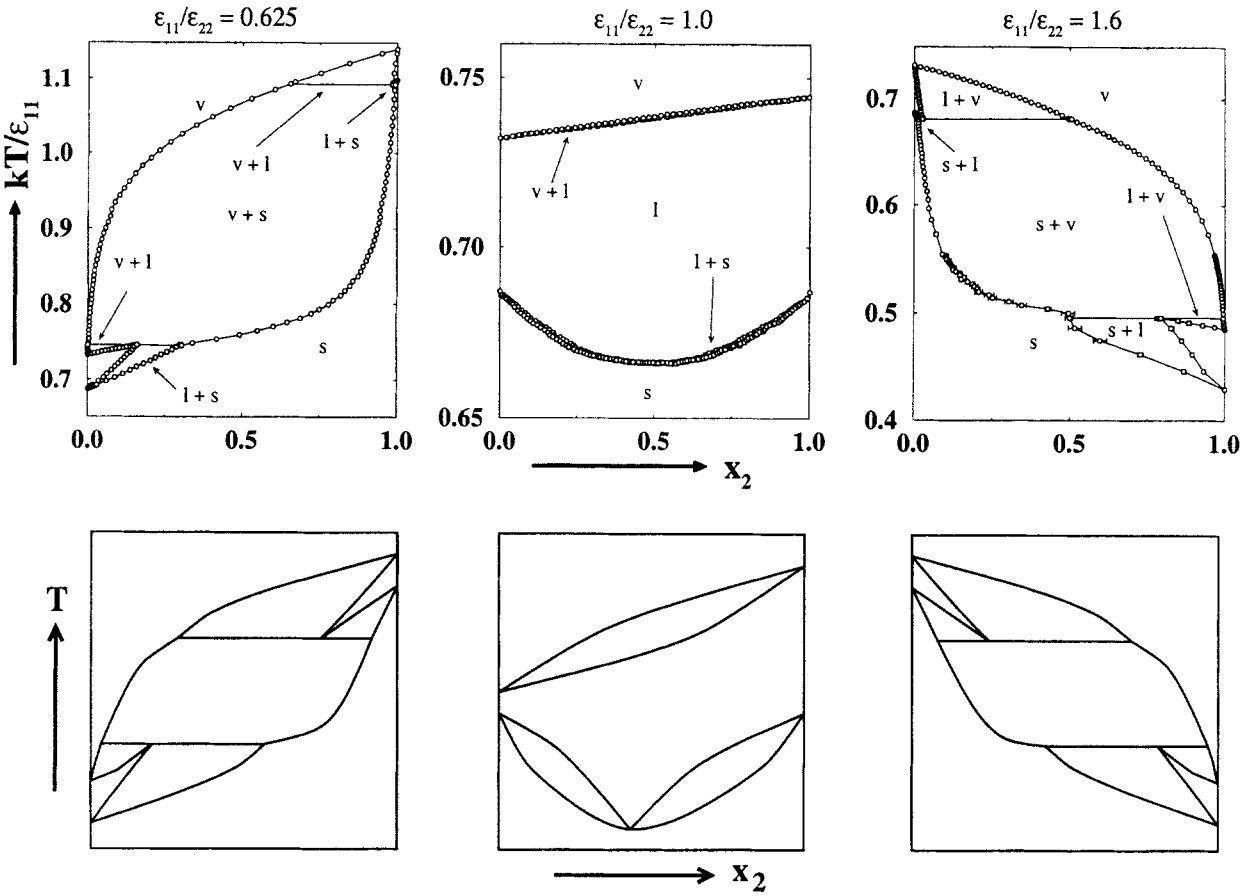


**Figure 2. Temperature vs. composition phase diagrams for Lennard-Jones binary mixtures with diameter ratio $\sigma_{11}/\sigma_{22} = 0.95$ at $P^* = 0.002$.**

Row 1 shows the phase diagrams obtained via Gibbs-Duhem integration. The circles represent data from Gibbs-Duhem integration simulations. Error bars are shown when they are larger than the width of the symbol. Lines are drawn through the points for clarity. The labels identifying the phases present in each region are as follows: v (vapor), l (liquid), and s (fcc solid solution). Row 2 gives diagrams (not to scale) corresponding to the phase diagrams in row 1.

curves. Solid-liquid coexistence lines originate from pure component 2 ($x_2 = 1$, $T^* = 0.687$) and decrease in temperature with decreasing fugacity fraction $\xi_2$ to a minimum melting point ($x_2 = 0.508$, $T^* = 0.666$). The solid-liquid lines then increase in temperature with decreasing fugacity fraction $\xi_2$ until they reach the solid-liquid coexistence temperature for pure component 1 ($x_2 = 0$, $T^* = 0.687$). A miscible solid phase exists below the solid-liquid curves.

On the phase diagram for $\sigma_{11}/\sigma_{22} = 0.95$ and $\epsilon_{11}/\epsilon_{22} = 1.6$, liquid-vapor coexistence lines originate from pure component 1 ($x_2 = 0$, $T^* = 0.732$) and decrease in temperature with increasing fugacity fraction $\xi_2$. Solid-liquid coexistence lines originate from pure component 1 ($x_2 = 0$, $T^* = 0.687$) and decrease in temperature with increasing fugacity fraction $\xi_2$. The liquid-vapor and solid-liquid curves meet at $T^* = 0.681$ and form a three-phase, solid-liquid-vapor equilibrium line. Solid-vapor coexistence lines originate from this three-phase line and decrease in temperature with increasing fugacity fraction $\xi_2$. Liquid-vapor coexistence lines originate from pure component 2 ($x_2 = 1$, $T^* = 0.485$) and increase in temperature with decreasing fugacity fraction $\xi_2$. The liquid-vapor and solid-vapor curves meet at $T^* = 0.495$ and form another three-phase, solid-liquid-vapor equilibrium line. Solid-liquid lines originate from this three-phase line and decrease in temperature with increasing fugacity fraction $\xi_2$ until they reach the solid-liquid coexistence temperature for pure component 2 ($x_2 = 0$, $T^* = 0.429$). A miscible solid phase exists below the solid-liquid curves.

For completeness, we present the phase diagrams for $\sigma_{11}/\sigma_{22} = 1.0$ and $\epsilon_{11}/\epsilon_{22} = 0.625$ and 1.6 in Figure 3. These phase diagrams are quite similar to the phase diagrams for $\sigma_{11}/\sigma_{22} = 0.95$ and $\epsilon_{11}/\epsilon_{22} = 0.625$ and 1.6. On the phase diagram for $\sigma_{11}/\sigma_{22} = 1.0$ and $\epsilon_{11}/\epsilon_{22} = 0.625$, vapor-liquid-solid equilibrium lines occur at $T^* = 1.096$ and $T^* = 0.738$. On the phase diagram for $\sigma_{11}/\sigma_{22} = 1.0$ and $\epsilon_{11}/\epsilon_{22} = 1.6$, vapor-liquid-solid equilibrium lines occur at $T^* = 0.681$ and $T^* = 0.490$.

In the second series, we calculated phase diagrams for binary mixtures with $\sigma_{11}/\sigma_{22} = 0.9$ and $\epsilon_{11}/\epsilon_{22} = 0.625$, 1.0, and 1.6. Figure 4 shows the temperature-composition phase diagrams obtained via Gibbs-Duhem integration (row 1) along with not-to-scale schematic diagrams (row 2). The phase diagram for $\sigma_{11}/\sigma_{22} = 0.9$ and $\epsilon_{11}/\epsilon_{22} = 0.625$ is similar to the phase diagram for $\sigma_{11}/\sigma_{22} = 0.95$ and $\epsilon_{11}/\epsilon_{22} = 0.625$ with vapor-liquid-solid equilibrium lines occurring at $T^* = 1.086$ and $T^* = 0.770$. However, the solid-liquid coexistence lines now have a minimum melting point; this occurs at $x_2 = 0.195$, $T^* = 0.665$. The phase diagram for $\sigma_{11}/\sigma_{22} = 0.9$ and $\epsilon_{11}/\epsilon_{22} = 1.0$ is similar to the phase diagram for $\sigma_{11}/\sigma_{22} = 0.95$ and $\epsilon_{11}/\epsilon_{22} = 1.0$, but now the minimum melting point in the solid-liquid coexistence lines occurs at $x_2 = 0.440$, $T^* = 0.593$.

The phase diagram for $\sigma_{11}/\sigma_{22} = 0.9$ and $\epsilon_{11}/\epsilon_{22} = 1.6$ is different from the phase diagram for $\sigma_{11}/\sigma_{22} = 0.95$ and $\epsilon_{11}/\epsilon_{22} = 1.6$, because now there is phase separation in the solid at low temperatures. Solid(1)-liquid-vapor equilibrium lines occur at $T^* = 0.679$ and $T^* = 0.505$, where solid(1) denotes an fcc disordered solid rich in component 1. Solid(1)-liquid lines originate from the three-phase line at $T^* = 0.505$ and decrease in temperature with increasing fugacity fraction $\xi_2$. Liquid-solid(2) coexistence lines, where solid(2) denotes an fcc disordered solid rich in component 2, originate from pure component 2 ($x_2 = 1$, $T^* = 0.429$) and increase in temperature with decreasing fugacity fraction $\xi_2$. The solid(1)-liquid and liquid-solid(2) curves meet at $T^* = 0.437$ and form a three phase, solid(1)-solid(2)-liquid equilibrium line. This line is also known as a peritectic. Below this temperature (not shown in Figure 4), solid(1) and solid(2) are in equilibrium. Although the Gibbs-Duhem integration method we employ

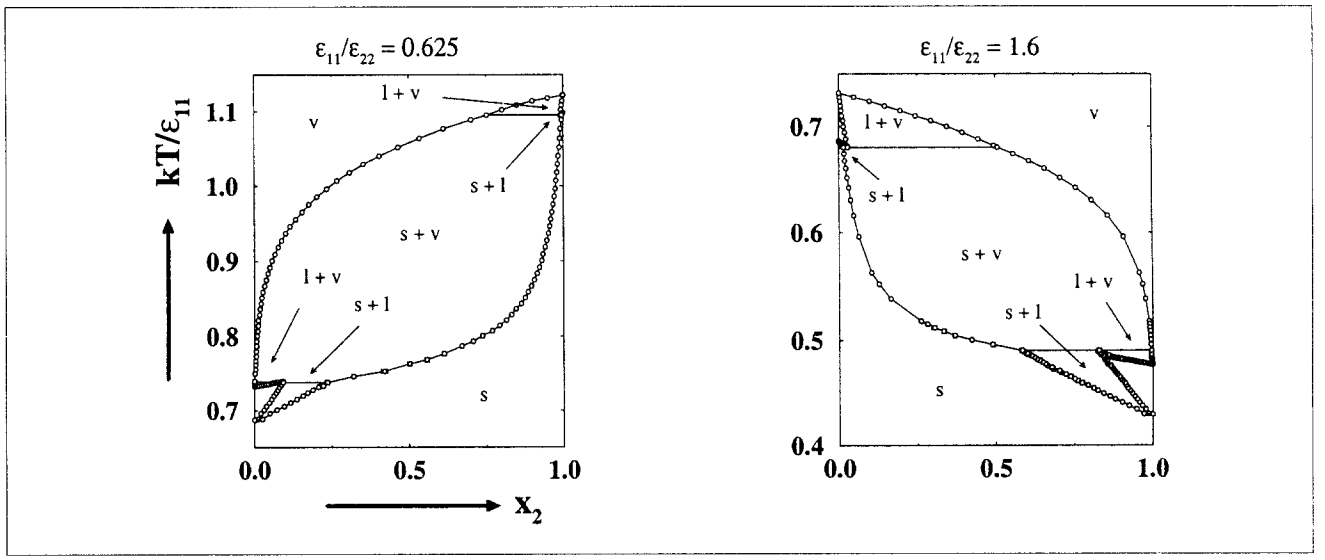


**Figure 3. Temperature vs. composition phase diagrams for Lennard-Jones binary mixtures with diameter ratio $\sigma_{11}/\sigma_{22} = 1.0$ at $P^* = 0.002$.**

The circles represent data from Gibbs-Duhem integration simulations. Error bars are shown when they are larger than the width of the symbol. Lines are drawn through the points for clarity. The labels identifying the phases present in each region are as follows: v (vapor), l (liquid), and s (fcc solid solution).

can be readily applied to solid-solid equilibria, we have not calculated solid(1)-solid(2) coexistence lines in this work since they are not necessary for classifying the solid-liquid behavior.

In the third series, we calculated phase diagrams for binary mixtures with $\sigma_{11}/\sigma_{22} = 0.85$ and $\epsilon_{11}/\epsilon_{22} = 0.625$, 1.0, and 1.6. Figure 5 shows the temperature-composition phase diagrams obtained via Gibbs-Duhem integration (row 1) along with not-to-scale diagrams (row 2). The phase diagram for $\sigma_{11}/\sigma_{22} = 0.85$ and $\epsilon_{11}/\epsilon_{22} = 0.625$ differs considerably from that at $\sigma_{11}/\sigma_{22} = 0.95$ and $\epsilon_{11}/\epsilon_{22} = 0.625$ in that it displays solid-phase separation at low temperatures. Vapor-liquid-solid(2) equilibrium lines occur at $T^* = 1.075$ and $T^* = 0.819$. The solid(1)-liquid and liquid-solid(2) curves form a eutectic at $x_2 = 0.345$, $T = 0.543$. On the phase diagram for $\epsilon_{11}/\epsilon_{22} = 1.0$, the solid(1)-liquid and liquid-solid(2) curves form a eutectic at $x_2 = 0.462$, $T^* = 0.466$. On the phase diagram for $\epsilon_{11}/\epsilon_{22} = 1.6$, vapor-liquid-solid(1) equilibrium lines occur at $T^* = 0.679$ and $T^* = 0.516$. The solid(1)-liquid and liquid-solid(2) curves form a eutectic at $x_2 = 0.928$, $T^* = 0.420$.

## Discussion

In this section, we discuss how the phase diagrams are influenced by variations in the intermolecular interactions. We then point out a number of real systems that display the same types of phase diagrams as those calculated for the Lennard-Jones binary mixtures in this work.

To understand how variations in the size and the attractive interactions lead to the complete phase diagrams displayed in Figures 2–5, it is helpful to consider the diagrams shown in Figure 6. The columns correspond to mixtures with diameter ratios $\sigma_{11}/\sigma_{22} = 0.95$, 0.9, and 0.85, and the rows correspond to mixtures with well-depth ratios $\epsilon_{11}/\epsilon_{22} = 1.6$, 1.0, and 0.625. The equilibrium curves for vapor-liquid, solid-liquid, and solid-vapor coexistence (black solid lines) are based on our simulation results. The equilibrium curves for solid-solid coexistence (gray solid lines) are based on our best guess as to how the upper critical solution temperature of the solid-solid immiscibility dome shifts with variations in the well-depth ratio. Underpinning this guess is quasichemical theory (Prince, 1966; Gordon, 1983) which tells us that the upper critical solution temperature increases as the attractions between like molecules become stronger than the attractions between unlike molecules, that is, for a constant $\sigma_{11}/\sigma_{22}$, the upper critical solution temperature will increase as $\epsilon_{11}/\epsilon_{22}$ increases above unity or decreases below unity, and, for a constant $\epsilon_{11}/\epsilon_{22}$, the upper critical solution temperature will increase as $\sigma_{11}/\sigma_{22}$ decreases. The metastable solid-liquid and vapor-liquid (black dashed lines) and the

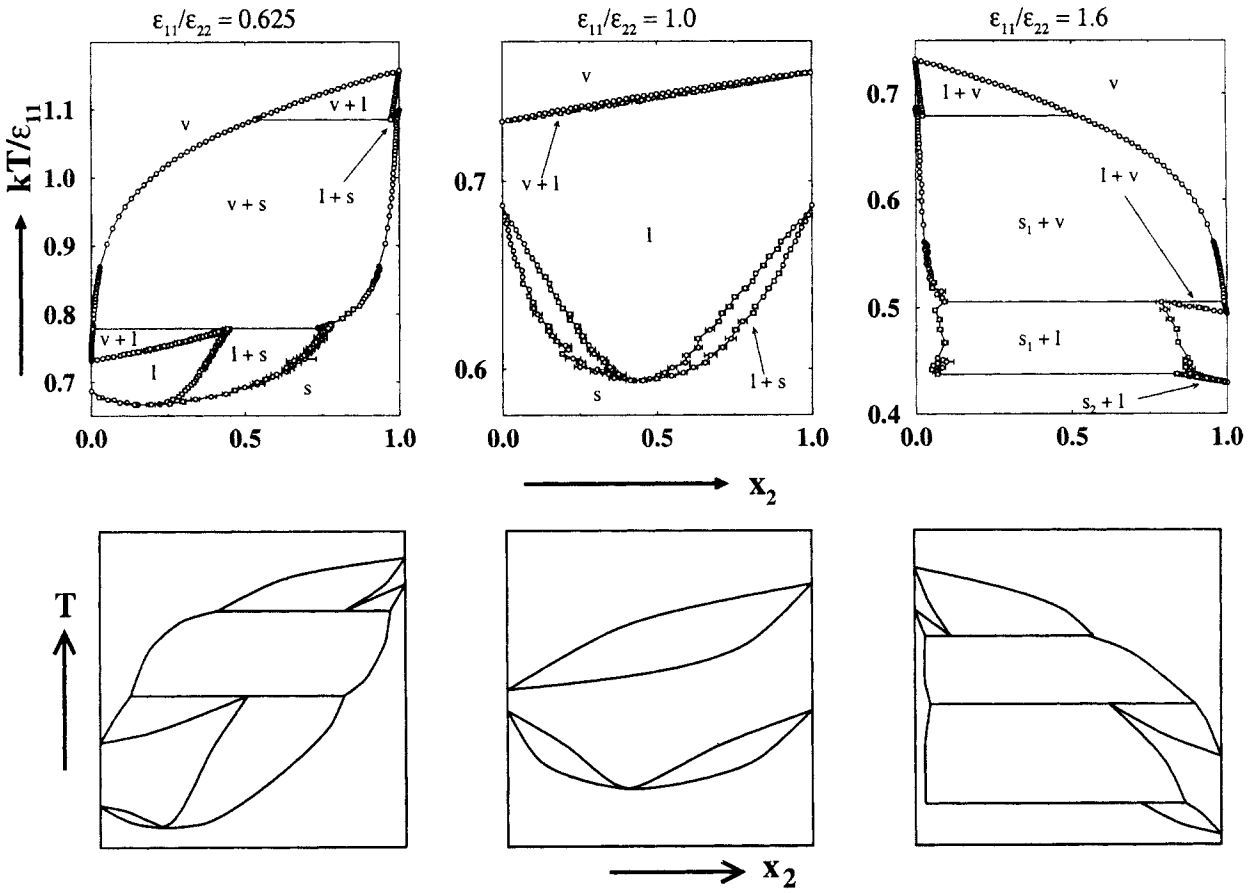


**Figure 4. Temperature vs. composition phase diagrams for Lennard-Jones binary mixtures with diameter ratio $\sigma_{11}/\sigma_{22} = 0.90$ at $P^* = 0.002$.**

Row 1 shows the phase diagrams obtained via Gibbs-Duhem integration. The labels $s_1$ and $s_2$ denote fcc solid solutions rich in component 1 and 2, respectively). Other symbols as in Figure 2. Row 2 gives schematic diagrams (not to scale) corresponding to the phase diagrams in row 1.

metastable solid-solid (gray dashed lines) coexistence curves are drawn to illustrate how these various two-phase coexistence regions interfere as diameter ratio and well-depth ratio are varied.

In the $\sigma_{11}/\sigma_{22} = 0.95$ column at $\epsilon_{11}/\epsilon_{22} = 1.0$, there are three, noninterfering two-phase coexistence regions: vapor-liquid, solid-liquid, and solid-solid. The solid-liquid coexistence region has a shape characteristic of a solid solution with a minimum melting point; this minimum melting point is inevitable since the melting temperatures of the pure components are equal (Rowlinson and Swinton, 1982). As the well-depth ratio increases to $\epsilon_{11}/\epsilon_{22} = 1.6$, the vapor-liquid and solid-liquid coexistence temperatures of pure component 2 decrease and the vapor-liquid and solid-liquid phase envelopes widen, causing them to interfere and form a vapor-solid coexistence region. Additionally, at $\epsilon_{11}/\epsilon_{22} = 1.6$, the difference between the melting temperatures of the pure components is sufficiently large that the minimum in the solid-liquid coexistence curve disappears and the shape of the solid-liquid coexistence region changes from a solid solution with a minimum melting point ($\epsilon_{11}/\epsilon_{22} = 1.0$) to a simple solid solution ($\epsilon_{11}/\epsilon_{22} = 1.6$). Likewise, as the well-depth ratio decreases to $\epsilon_{11}/\epsilon_{22} = 0.625$, the vapor-liquid and solid-liquid coexistence temperatures of pure component 2 increase, resulting in a similar pattern of vapor-liquid, solid-liquid interference and a change in the shape of the solid-liquid coexistence region from a solid solution with a minimum melting point ($\epsilon_{11}/\epsilon_{22} = 1.0$) to a simple solid solution ($\epsilon_{11}/\epsilon_{22} = 0.625$).

In the $\sigma_{11}/\sigma_{22} = 0.90$ column, at $\epsilon_{11}/\epsilon_{22} = 1.0$, there are again three, noninterfering two-phase coexistence regions: vapor-liquid, solid-liquid, and solid-solid. The solid-liquid coexistence region has a shape characteristic of a solid solution with a minimum melting point. As the well-depth ratio increases to $\epsilon_{11}/\epsilon_{22} = 1.6$, the vapor-liquid and solid-liquid coexistence temperatures of pure component 2 decrease and the vapor-liquid and solid-liquid phase envelopes widen, causing them to interfere and form a vapor-solid coexistence region. Additionally, at $\epsilon_{11}/\epsilon_{22} = 1.6$, the difference between the melting temperatures of the pure components is sufficiently large that the minimum in the solid-liquid coexistence curve disappears, however, instead of forming a simple solid solution shape (as was the case for $\sigma_{11}/\sigma_{22} = 0.95$, $\epsilon_{11}/\epsilon_{22} = 1.6$), the solid-liquid coexistence region displays a shape characteristic of a peritectic. This peritectic shape can be thought of as resulting from the interference between a solid-liquid coexistence region with a solid solution shape and a solid-solid immiscibility dome, as shown by the dashed curves. Likewise,

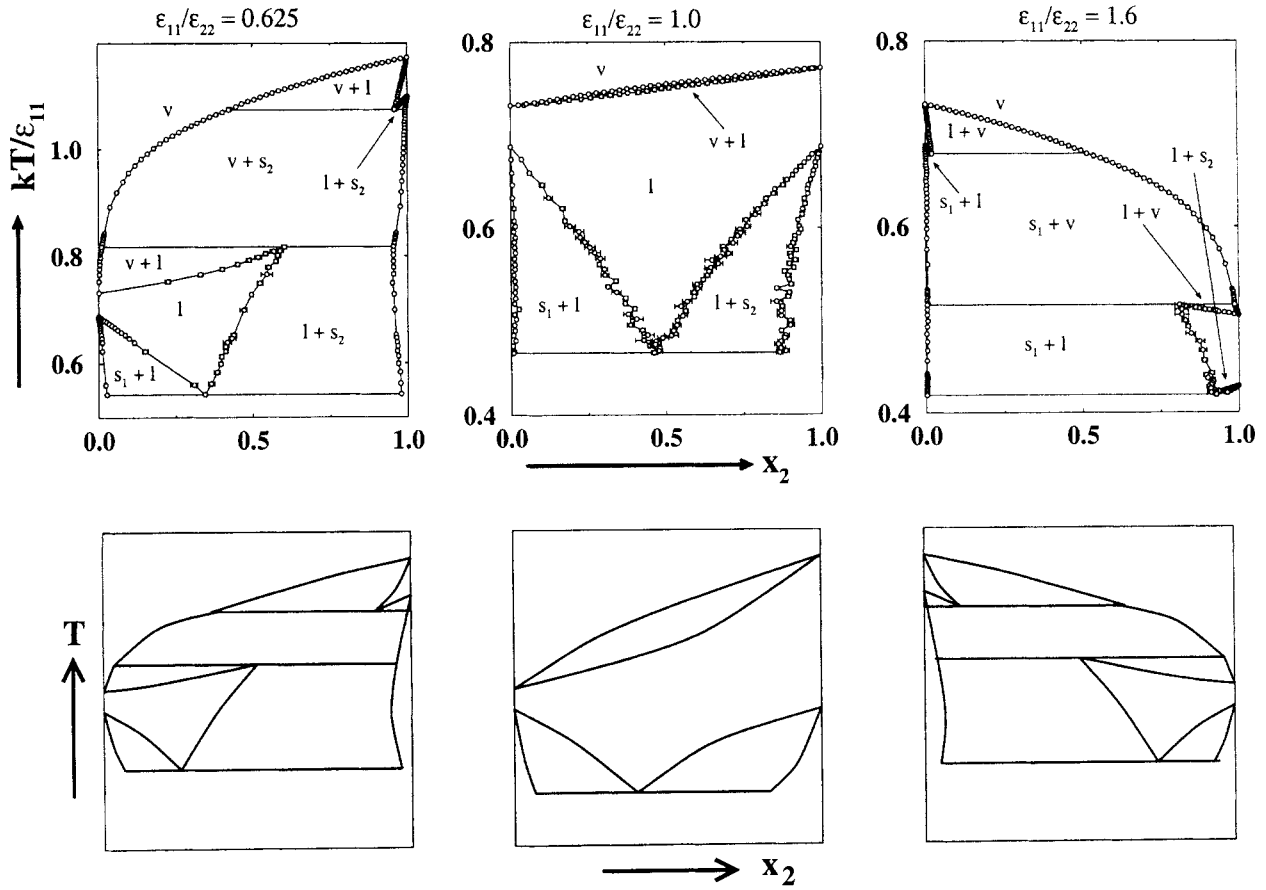


**Figure 5. Temperature vs. composition phase diagrams for Lennard-Jones binary mixtures with diameter ratio $\sigma_{11}/\sigma_{22} = 0.85$ at $P^* = 0.002$.**

Row 1 shows the phase diagrams obtained via Gibbs-Duhem integration. The labels $s_1$ and $s_2$ denote fcc solid solutions rich in component 1 and 2, respectively). Other symbols as in Figure 2. Row 2 gives diagrams (not to scale) corresponding to the phase diagrams in row 1.

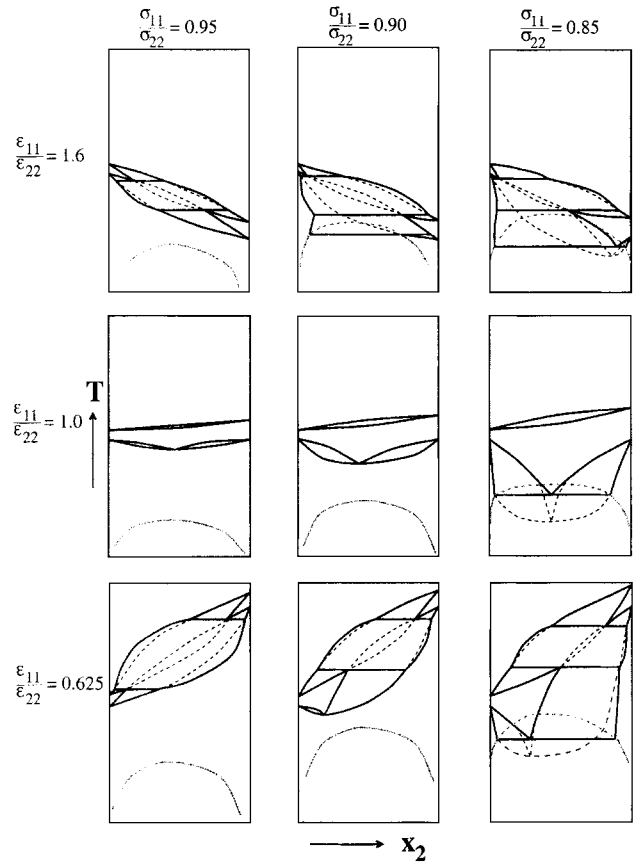


**Figure 6. Interference between vapor-liquid, solid-liquid and solid-solid coexistence regions.**

The columns correspond to mixtures with diameter ratios $\sigma_{11}/\sigma_{22} = 0.95$, 0.9, and 0.85, and the rows correspond to mixtures with well-depth ratios $\epsilon_{11}/\epsilon_{22} = 1.6$, 1.0, and 0.625. Solid black lines correspond to equilibrium curves calculated in this work. Solid gray lines represent solid-solid coexistence curves, which have not been calculated for these mixtures, but have been estimated using quasichemical theory. Metastable coexistence curves are indicated with dashed lines.

as the well-depth ratio decreases to $\epsilon_{11}/\epsilon_{22} = 0.625$, the vapor-liquid and solid-liquid coexistence temperatures of pure component 2 increase, resulting in a similar pattern of vapor-liquid, solid-liquid interference. Here, the solid-liquid coexistence region retains its solid solution with a minimum melting temperature shape.

In the $\sigma_{11}/\sigma_{22} = 0.85$ column at $\epsilon_{11}/\epsilon_{22} = 1.0$, there is a noninterfering vapor-liquid coexistence region followed at lower temperatures by a solid-liquid coexistence region with a shape characteristic of a eutectic. This eutectic shape can be thought of as resulting from the interference between a solid-liquid coexistence region with a minimum melting temperature and a solid-solid immiscibility dome, as shown by the dashed curves. As the well-depth ratio increases to $\epsilon_{11}/\epsilon_{22} = 1.6$, the vapor-liquid and solid-liquid coexistence temperatures of pure component 2 decrease and the vapor-liquid and solid-liquid phase envelopes widen, causing them to interfere and form a vapor-solid coexistence region. The shape of the solid-liquid coexistence region remains the same, although the eutectic composition (the point at which the two liquid-phase lines cross) shifts towards pure component 2. Likewise, as the well-depth ratio decreases to $\epsilon_{11}/\epsilon_{22} = 0.625$, the vapor-liquid and solid-liquid coexistence temperatures of pure component 2 increase, resulting in a similar pattern of vapor-liquid, solid-liquid interference. Again, the shape of the solid-liquid coexistence region remains the same, but here the eutectic composition shifts towards pure component 1.

In the $\epsilon_{11}/\epsilon_{22} = 1.0$ row, there is no interference between the vapor-liquid and solid-liquid coexistence regions. As $\sigma_{11}/\sigma_{22}$ decreases, the vapor-liquid coexistence temperature of pure component 2 increases and the vapor-liquid phase envelope widens. At $\sigma_{11}/\sigma_{22} = 0.95$, there is a minimum melting temperature in the solid-liquid coexistence region. As $\sigma_{11}/\sigma_{22}$ decreases, the solid-liquid lines "fall" because the liquid phase can accommodate the larger differences in size easier than the solid phase (Hume-Rothery et al., 1969); this results in the minimum melting temperature decreasing with decreasing $\sigma_{11}/\sigma_{22}$. At $\sigma_{11}/\sigma_{22} = 0.85$, the minimum melting temperature is below the upper critical solution temperature of the solid-solid coexistence region and a eutectic line is formed. Similar trends can be observed in the $\epsilon_{11}/\epsilon_{22} = 0.625$ and 1.6 rows.

It is of interest to determine which real binary mixtures display phase diagrams that are qualitatively similar to the phase diagrams for the Lennard-Jones binary mixtures shown in Figures 2–5. We make these comparisons with the full understanding that the Lennard-Jones potential is not necessarily a suitable model for many of the real systems mentioned below. Nevertheless, it is interesting to see what molecular features the real mixture and the Lennard-Jones mixture have in common since this helps us to gain insight into how molecular properties affect phase behavior.

The binary mixture *p*-dichlorobenzene-*p*-dibromobenzene is expected to display a $T - x$ phase diagram with the same qualitative features as in the diagram for $\sigma_{11}/\sigma_{22} = 0.95$ and $\epsilon_{11}/\epsilon_{22} = 0.625$. We say "expected" here, because no $T - x$ phase diagram has been published for this mixture. Based on the experimental measurements of the solid-liquid-vapor coexistence line (Kruyt, 1912) and the fact that this mixture has been found to form solid solutions (Walsh and Smith, 1961; de Kruif et al., 1981) one can deduce that a $T - x$ diagram like the one shown on the lefthand side of Figure 2 should be observed at a pressure slightly above the triple point pressure of *p*-dibromobenzene. The similarities in phase behavior between the real mixture and the Lennard-Jones mixture can be explained by noting that both *p*-dichlorobenzene and *p*-dibromobenzene are symmetric molecules and that they differ in size by approximately 6% along their longest linear dimension (Remyga et al., 1971).

At atmospheric pressure, the binary mixture argon-methane is expected to display a $T - x$ phase diagram with the same qualitative features as in the diagram for $\sigma_{11}/\sigma_{22} = 0.9$ and $\epsilon_{11}/\epsilon_{22} = 1.0$ (Figure 4, middle). Again, we say "expected" because there are no published $T - x$ measurements of the vapor-liquid region at atmospheric pressure. Nevertheless, based on constant-temperature $P - x$ measurements (Sprow and Prausnitz, 1966), it is reasonable to expect that the $T - x$ vapor-liquid equilibrium will be spindle-shaped as in Figure 4 (middle), because the $P - x$ vapor-liquid region forms a spindle shape. The solid-liquid coexistence curves for argon-methane at atmospheric pressure were determined experimentally by van't Zelfde et al. (1968). Subsequent measure-

ments by Greer et al. (1969) showed that a solid-solid immiscibility gap exists directly below the solid-liquid curve. According to the Lennard-Jones parameters determined by Clifford et al. (1977) from viscosity data, the argon-methane mixture has a diameter ratio $\sigma_{Ar}/\sigma_{CH_4} = 0.9$ and a well-depth ratio $\epsilon_{Ar}/\epsilon_{CH_4} = 0.88$. Upon comparing these parameters with the parameters above, it appears that the diameter ratio of the two components has more influence on the phase diagram than the well-depth ratio.

Aqueous salt systems, such as $H_2O$-NaCl, $H_2O$-$AgNO_3$, and $H_2O$-$KNO_3$ (Ricci, 1951; Zernike, 1955), display $T-x$ phase diagrams with the same qualitative features as in the diagram for $\sigma_{11}/\sigma_{22} = 0.85$ and $\epsilon_{11}/\epsilon_{22} = 0.625$ (Figure 5, lefthand side). The binary mixture methane-*n*-hexadecane also displays this type of $T-x$ phase diagram at pressures between the triple point of methane and the critical point of *n*-hexadecane (Glaser et al., 1985). The common characteristic among all these real systems is that there is a relatively large difference between the pure component coexistence temperatures, which is reflected in the Lennard-Jones mixture by the large well-depth ratio since temperature scales with the well-depth parameter. The binary mixture iodine-sulfur (Okamoto, 2000) displays a $T-x$ phase diagram with the same qualitative features as the diagram for $\sigma_{11}/\sigma_{22} = 0.85$ and $\epsilon_{11}/\epsilon_{22} = 1.0$. The similarities in phase behavior between a mixture of iodine and sulfur and the Lennard-Jones mixture can be explained by noting that the melting points of iodine and sulfur are nearly identical, (that is, the well-depth ratio of this mixture is unity), while their size difference is about 20%.

## Summary

The Gibbs-Duhem integration technique was combined with semigrand canonical Monte Carlo simulations to calculate complete $T-x$ phase diagrams for binary Lennard-Jones mixtures. To explore the effect of molecular size and intermolecular attractions on the complete phase behavior of a mixture, we calculated phase diagrams for binary Lennard-Jones mixtures with diameter ratios ranging from $0.85-1$ and attractive well-depth ratios ranging from $0.625-1.6$, at a reduced pressure $P^* = 0.002$.

These calculations mark the first time that molecular simulation has been used to obtain phase diagrams describing all types of equilibria between vapor, liquid, and solid phases. This capability affords the possibility of classifying phase diagrams based not only on fluid-phase behavior, as was done by van Konynenburg and Scott, but also on solid phase behavior. The Gibbs-Duhem integration approach holds a few advantages over the equation of state approach for calculating phase equilibria: (1) equations of state do not allow for solid-phase formation, but a solid phase with any crystalline structure can be readily incorporated into the Gibbs-Duhem integration scheme; (2) equation of state predictions may produce unrealistic phase behavior due to the approximations that are made when developing an analytical equation of state for a particular molecular model, while the Gibbs-Duhem integration predictions are based on simulation results, which are exact for the molecular model under study (Allen and Tildesley, 1987).

The limitations of this approach should be pointed out as well. First, the Gibbs-Duhem integration procedure, as formulated here, cannot be used to evaluate critical phenomena. Second, it is not always trivial to obtain an initial condition to begin the integration. For example, there is presently no straightforward way to begin a Gibbs-Duhem integration calculation of liquid-liquid or solid-solid coexistence lines that are not connected (via a heteroazeotrope or eutectic) to a pure component coexistence point. In principle, one could conduct a Gibbs ensemble simulation to obtain an initial coexistence condition for liquid-liquid equilibria, but often the densities of the liquid phases are too high to permit a sufficient number of successful particle transfers. An alternative approach would entail conducting Gibbs-Duhem integration simulations at some lower pressure where the vapor-liquid and liquid-liquid coexistence regions meet at a heteroazeotrope. Using the liquid-liquid coexistence points from the heteroazeotrope at the lower pressure, a constant temperature Gibbs-Duhem integration could then be conducted to determine a liquid-liquid coexistence point at the desired pressure. This liquid-liquid coexistence point then becomes the initial condition for the Gibbs-Duhem integration of the full liquid-liquid coexistence curve. Calculations of this nature are currently underway.

## Acknowledgments

We gratefully acknowledge J. M. H. Levelt Sengers for directing us to the papers by Bakhuis Roozeboom and Buchner, and Smits. This work was supported by the GAANN Computational Sciences Fellowship of the U.S. Dept. of Education and the Office of Energy Research, Basic Sciences, Chemical Science Division of the U.S. Dept. of Energy under Contract No. DE-FG05-91ER14181. Acknowledgment is made to the Donors of the Petroleum Research Fund administered by the American Chemical Society for partial support of this work.

## Literature Cited

Allen, M. P., and D. J. Tildesley, *Computer Simulation of Liquids*, Clarendon Press, Oxford (1987).

Agrawal, R., and D. A. Kofke, "Thermodynamic and Structural Properties of Model Systems at Solid-Fluid Coexistence: II. Melting and Sublimation of the Lennard-Jones System," *Molec. Phys.*, **85**, 43 (1995).

Bakhuis Roozeboom, H. W., and E. H. Buchner, "Critical Terminating Points in Three-Phase Lines with Solid Phases in Binary Systems Which Present Two Liquid Layers," *Proc. of Koninklijke Akademie van Wetenschappen*, **7**, 556 (1905).

Barrat, J. L., M. Baus, and J. P. Hansen, "Density-Functional Theory of Freezing of Hard-Sphere Mixtures in Substitutional Solid Solutions," *Phys. Rev. Lett.*, **56**, 1063 (1986).

Barrat, J. L., M. Baus, and J. P. Hansen, "Freezing of Hard-Sphere Mixtures into Disordered Crystals: A Density-Functional Approach," *J. Phys. C: Solid State Phys.*, **20**, 1413 (1987).

Canongia Lopes, J. N., "Phase Equilibria in Binary Lennard-Jones Mixtures: Phase Diagram Simulation," *Molec. Phys.*, **96**, 1649 (1999).

Canongia Lopes, J. N., and D. J. Tildesley, "Multiphase Equilibria Using the Gibbs Ensemble Method," *Molec. Phys.*, **92**, 187 (1997).

Carnahan, B., H. A. Luther, and J. O. Wilkes, *Applied Numerical Methods*, Wiley, New York (1969).

Clifford, A. A., P. Gray, and N. Platts, "Lennard-Jones 12:6 Parameters for Ten Small Molecules," *J. Chem. Soc. Faraday Trans. I*, **73**, 381 (1977).

Cottin, X., and P. A. Monson, "Substitutionally Ordered Solid Solutions of Hard Spheres," *J. Chem. Phys.*, **102**, 3354 (1995).

Deiters, U. K., and I. L. Pegg, "Systematic Investigation of the Phase Behavior in Binary Fluid Mixtures: I. Calculations Based on the

Redlich-Kwong Equation of State," *J. Chem. Phys.*, **90**, 6632 (1989).
de Kruif, C. G., A. C. G. van Genderen, J. C. W. G. Bink, and H. A. J. Oonk, "Properties of Mixed Crystalline Organic Material Prepared by Zone Levelling: II. Vapour Pressure and Excess Gibbs Energies of ( *p*-Dichlorobenzene + *p*-Dibromobenzene)," *J. Chem. Thermody.*, **13**, 457 (1981).
Garcia, D. C., and K. D. Luks, "Patterns of Solid-Fluid Phase Equilibria: New Possibilities?," *Fluid Phase Equil.*, **161**, 91 (1999).
Georgoulaki, A. M., I. V. Ntouros, D. P. Tassios, and A. Z. Panagiotopoulos, "Phase Equilibria of Binary Lennard-Jones Mixtures: Simulation and Van der Waals 1-Fluid Theory," *Fluid Phase Equil.*, **100**, 153 (1994).
Glaser, M., C. J. Peters, H. J. van der Kooi, and R. N. Lichtenthaler, "Phase Equilibria (Methane + *n*-Hexadecane) and ($p,V_m,T$) of *n*-Hexadecane," *J. Chem. Thermody.*, **17**, 803 (1985).
Gordon, P., *Principles of Phase Diagrams in Materials Systems*, Krieger, Malabar, FL (1983).
Greer, S. C., L. Meyer, and C. S. Barrett, "Argon-Methane Phase Diagram," *J. Chem. Phys.*, **50**, 4299 (1969).
Guo, M., Y. Li, Z. Li, and J. Lu, "Molecular Simulation of Liquid-Liquid Equilibria for Lennard-Jones Fluids," *Fluid Phase Equil.*, **98**, 129 (1994).
Hansen, J. P., and L. Verlet, "Phase Transitions of the Lennard-Jones System," *Phys. Rev.*, **184**, 151 (1969).
Harismiadis, V. I., N. K. Kourtras, D. P. Tassios, and A. Z. Panagiotopoulos, "How Good is Conformal Solutions Theory for Binary Phase Equilibrium Predictions?," *Fluid Phase Equil.*, **65**, 1 (1991).
Hitchcock, M. R., and C. K. Hall, "Solid-Liquid Phase Equilibrium for Binary Lennard-Jones Mixtures," *J. Chem. Phys.*, **110**, 11433 (1999).
Hitchcock, M. R., and C. K. Hall, "Complete Phase Diagrams for Binary Mixtures via Gibbs-Duhem Integration," *Proc. of Foundations of Molecular Modeling and Simulation Conf.* (2000).
Hume-Rothery, W., R. E. Smallman, and C. W. Hayworth, *The Structure of Metals and Alloys*, The Metals and Metallurgy Trust, London (1969).
Kofke, D. A., "Solid-Fluid Coexistence in Binary Hard Sphere Mixtures by Semigrand Monte Carlo Simulation," *Molec. Simul.*, **7**, 285 (1991).
Kofke, D. A., "Direct Evaluation of Phase Coexistence by Molecular Simulation via Integration Along the Saturation Line," *J. Chem. Phys.*, **98**, 4149 (1993).
Kofke, D. A., "Semigrand Canonical Monte Carlo Simulation. Integration Along Coexistence Lines," *Adv. Chem. Phys.*, **105**, 405 (1998).
Kofke, D. A., and E. D. Glandt, "Monte Carlo Simulations of Multicomponent Equilibria in a Semigrand Canonical Ensemble," *Molec. Phys.*, **64**, 1105 (1988).
Kranendonk, W. G. T., and D. Frenkel, "Computer Simulation of Solid-Liquid Coexistence in Binary Hard-Sphere Mixtures," *Molec. Phys.*, **72**, 679 (1991).
Kraska, T., and U. K. Deiters, "Systematic Investigation of the Phase Behavior in Binary Fluid Mixtures: II. Calculations Based on the Carnahan-Starling-Redlich-Kwong Equation of State," *J. Chem. Phys.*, **96**, 539 (1992).
Kruyt, H., "Das Gleichgewicht Fest-Flussig-Gas in Binaren Mischkristallsystemen," *Z. Physik. Ch.*, **79**, 42 (1912).
Labadie, J. A., D. C. Garcia, and K. D. Luks, "Patterns of Solid-Fluid Phase Equilibria II. Interplay with Fluid Phase Criticality and Stability," *Fluid Phase Equil.*, **171**, 11 (2000).
Lamm, M. H., and C. K. Hall, "Monte Carlo Simulations of Complete Phase Diagrams for Binary Lennard-Jones Mixtures," *Fluid Phase Equil.*, in press (2000).
Luks, K. D., "Experimental Techniques in Solid-Liquid Equilibrium," *Proc. of 2nd Int. Conf. on Phase Equil. and Fluid Properties in the Chem. Ind.*, EFCE Series No. 11, Part II, 699 (1980).
Mazur, V. A., L. Z. Boshkov, and V. G. Murakhovsky, "Global Phase Behavior of Binary Mixtures of Lennard-Jones Molecules," *Phys. Lett.*, **104**, 415 (1984).
Mehta, M., and D. A. Kofke, "Coexistence Diagrams of Mixtures by Molecular Simulation," *Chem. Eng. Sci.*, **49**, 2633 (1994).
Okamoto, H., "I-S(Iodine-Sulfur)," *J. Phase Equil.*, **21**, 109 (2000).
Panagiotopoulos, A. Z., "Direct Determination of Phase Coexistence Properties of Fluids by Monte Carlo Simulation in a New Ensemble," *Mol. Phys.*, **61**, 813 (1987).
Panagiotopoulos, A. Z., N. Quirke, M. Stapleton, and D. J. Tildesley, "Phase Equilibria by Simulation in the Gibbs Ensemble," *Mol. Phys.*, **63**, 527 (1988).
Panagiotopoulos, A. Z., "Monte Carlo Methods for Phase Equilibria of Fluids" *J. Phys.: Condens. Matter*, **12**, R25 (2000).
Peters, C. J., R. N. Lichtenthaler, and J. de Swaan Arons, "Three Phase Equilibria in Binary Mixtures of Ethane and Higher Alkanes" *Fluid Phase Equil.*, **29**, 495 (1986).
Prince, A., *Alloy Phase Equilibria*, Elsevier, Amsterdam (1966).
Remyga, S. A., R. M. Myasnikova, and A. I. Kitaigorodskii, "Phase Diagrams for the Ternary Organic Systems *p*-Dibromobenzene-*p*-Chloronitrobenzene-*p*-Bromonitrobenzene and *p*-Dibromobenzene-*p*-Chloronitrobenzene-*p*-Dichlorobenzene," *Russ. J. Phys. Chem*, **45**, 328 (1971).
Ricci, J. E., *The Phase Rule and Heterogeneous Equilibrium*, Van Nostrand, London (1951).
Rowlinson, J. S., and F. L. Swinton, *Liquids and Liquid Mixtures*, Butterworth Scientific, London (1982).
Sadus, R. J., "Molecular Simulation of the Phase Behavior of Ternary Fluid Mixtures: the Effect of a Third Component on Vapor-Liquid and Liquid-Liquid Coexistence," *Fluid Phase Equil.*, **157**, 169 (1999).
Schneider, G. M., "Phase Equilibria in Fluid Mixtures at High Pressures," *Adv. Chem. Phys.*, **17**, 1 (1970).
Schneider, G. M., "High-Pressure Phase Diagrams and Critical Properties of Fluid Mixtures," *Chemical Thermodynamics*, Vol. 2, Specialist Periodical Report, M. L. McGlashan, ed., The Chemical Society, London (1978).
Scott, R. L., "Models for Phase Equilibria in Fluid Mixtures," *Acc. Chem. Res.*, **20**, 97 (1987).
Scott, R. L., and P. H. van Konynenburg, "Van der Waals and Related Models for Hydrocarbon Mixtures," *Discuss. Faraday Soc.*, **49**, 87 (1970).
Smits, A., "The Course of the Solubility Curve in the Region of Critical Temperatures of Binary Mixtures," *Proc. of Koninklijke Akademie van Wetenschappen*, **6**, 171 (1903).
Sprow, F. B., and J. M. Prausnitz, "Vapor-Liquid Equilibria for Five Cryogenic Mixtures," *AIChE J.*, **12**, 780 (1966).
Tsang, P. C., O. M. White, B. Y. Perigard, L. F. Vega, and A. Z. Panagiotopoulos, "Phase Equilibria of Ternary Lennard-Jones Systems," *Fluid Phase Equil.*, **107**, 31 (1995).
Valyashko, V. M., "Complete Phase Diagrams of Binary Systems with Different Volatility Components," *Z. Phys. Chemie, Leipzig*, **267**, 481 (1986).
Valyashko, V. M., "Sub- and Supercritical Equilibria in Aqueous Electrolyte Solutions," *Pure & Appl. Chem.*, **62**, 2129 (1990).
van Konynenburg, P. H., and R. L. Scott, "Critical Lines and Phase Equilibria in Binary van der Waals Mixtures," *Phil. Trans. Roy. Soc. London (A)*, **298**, 495 (1980).
van Leeuwen, M. E., C. J. Peters, J. de Swaan Arons, and A. Z. Panagiotopoulos, "Investigation of the Transition to Liquid-Liquid Immiscibility for Lennard-Jones (12,6) Systems, Using Gibbs-Ensemble Molecular Simulations," *Fluid Phase Equil.*, **66**, 57 (1991).
Vlot, M. J., J. C. van Miltenburg, H. A. J. Oonk, and J. P. van der Eerden, "Phase Diagrams of Scalemic Mixtures: A Monte Carlo Simulation Study," *J. Chem. Phys.*, **107**, 10102 (1997).
Walsh, P. N., and N. O. Smith, "Sublimation Pressure of Solid Solutions: II. The Systems *p*-Dichlorobenzene-*p*-Dibromobenzene, *p*-Dichlorobenzene-*p*-Bromochlorobenzene, and *p*-Dibromobenzene-*p*-Bromochlorobenzene at 50 C," *J. Phys. Chem.*, **65**, 718 (1961).
Wang, J. L., G. W. Wu, and R. J. Sadus, "Closed-Loop Liquid-Liquid Equilibria and the Global Phase Behaviour of Binary Mixtures Involving Hard-Sphere + van der Waals Interactions," *Molec. Phys.*, **98**, 715 (2000).
van't Zelfde, P., M. H. Omar, H. G. M. le Pair-Schroten, and Z. Dokoupil, "Solid-Liquid Equilibrium Diagram for the Argon-Methane System," *Physica*, **38**, 241 (1968).
Zernike, J., *Chemical Phase Theory*, Kluwer, Deventer (1955).

*Manuscript received Nov. 22, 2000, and revision received Mar. 9, 2001.*